

Full length article

A multimaterial sensor with Janus characteristics based on enhanced particle swarm optimization algorithm

Jie Xu, Zhao Tang, Jun-Yang Sui, Hai-Feng Zhang*

College of Electronic and Optical Engineering & College of Flexible Electronics, Nanjing University of Posts and Telecommunications, Jiangsu Province 210023, China

ARTICLE INFO

Keywords:

Janus characteristics
Layered photonic structures
Defect modes
Pressure sensing
Enhanced particle swarm optimization algorithm

ABSTRACT

This paper presents an enhanced particle swarm optimization (EPSO) algorithm for optimizing the parameters of a layered photonic structure. By dynamically adjusting the thickness and refractive index of each dielectric layer, the phase and absorption properties of the transmitted electromagnetic waves (EWs) can be modified, effectively achieving high absorption rates by incorporating defects formed by the Kerr nonlinear material. The proposed EPSO algorithm facilitates the identification of the global optimal solution, resulting in the formation of sharp absorption peaks with values exceeding 0.9 for incident EWs from various directions. Leveraging the Janus properties, the EW exhibits distinct physical characteristics when incident from the front and back directions, enabling the creation of sensors tailored for thickness, angle, and pressure sensing. The forward angle sensing demonstrates a high sensitivity (S) of 0.32 nm/degree, a quality factor (Q) of 543.9, and a figure of merit (FOM) of 0.32 degree⁻¹. Both pressure and thickness can be sensed in both forward and backward directions, with S of 5.46 nm/GPa and 10.24 nm/GPa, mean Q of 563.9 and 316.7, and FOM of 5.5 GPa⁻¹ and 3.3 GPa⁻¹, respectively. Thus, it can be stated that the proposed EPSO holds promising prospects for optical sensor design.

1. Introduction

The layered photonic structure (LPS) is popular in current research, which represents a novel class of metamaterials that harnesses unique physical properties, such as photonic band gaps and energy localization, enabling precise control of photons [1–3]. When arranged periodically, the LPS exhibits a pronounced contrast before and after the propagation of electromagnetic waves (EWs), giving rise to distinctive physical phenomena.

Certainly, the design features of LPS, encompassing absorber and polarization converter elements, exhibit remarkable performance. [4–5]. Among various applications, LPS has gained popularity in sensor design [6–7]. While existing sensors have found utility in cancer cell detection, air quality monitoring, and ambient temperature measurement [8–10], research on pressure sensors remains limited. Pressure sensors operate based on the refractive index (RI) principle, as different piezoresistive materials possess distinct strain optical coefficients, also known as photo-elastic constants. These coefficients describe the relationship between strain and birefringence, the property of splitting light into two beams with different polarization states upon passing through a material. When subjected to mechanical stress or strain, the RI of a

material changes, thereby influencing its birefringence. Traditional sensor designs often restrict measurements to a single variable, not many physical quantities, and no Janus effect, presenting limitations in practical production processes [11]. Inspired by Janus, the Roman god depicted with two faces—one looking to the past and the other to the future—the concept of Janus is introduced into the field of physics [12]. In the context of sensors, Janus describes the unique sensing properties observed when EWs come from different directions [13].

Prior research has demonstrated the utilization of intrinsic absorption and optical Tamm states of graphene to create sharp absorption peaks [14–15], where defect modes have emerged as the prevailing approach [16]. By incorporating defect films into the LPS, the regular periodic arrangement of the structure can be disrupted, leading to the formation of localized optical defects and the introduction of novel band structures. Through appropriate adjustments of the defective film's thickness and RI, optical waveguide and interference effects arise when it interacts with the surrounding media, ultimately resulting in the formation of sharp absorption peaks within specific wavelength ranges. Currently, most pressure sensors in research lack the Janus characteristics of bidirectional measurement, restricting their capabilities to measure a single direction. Moreover, they are limited to detecting only

* Corresponding author.

E-mail addresses: hanlor@njupt.edu.cn, hanlor@163.com (H.-F. Zhang).

<https://doi.org/10.1016/j.optlastec.2023.110242>

Received 22 July 2023; Received in revised form 4 October 2023; Accepted 17 October 2023

Available online 20 October 2023

0030-3992/© 2023 Elsevier Ltd. All rights reserved.

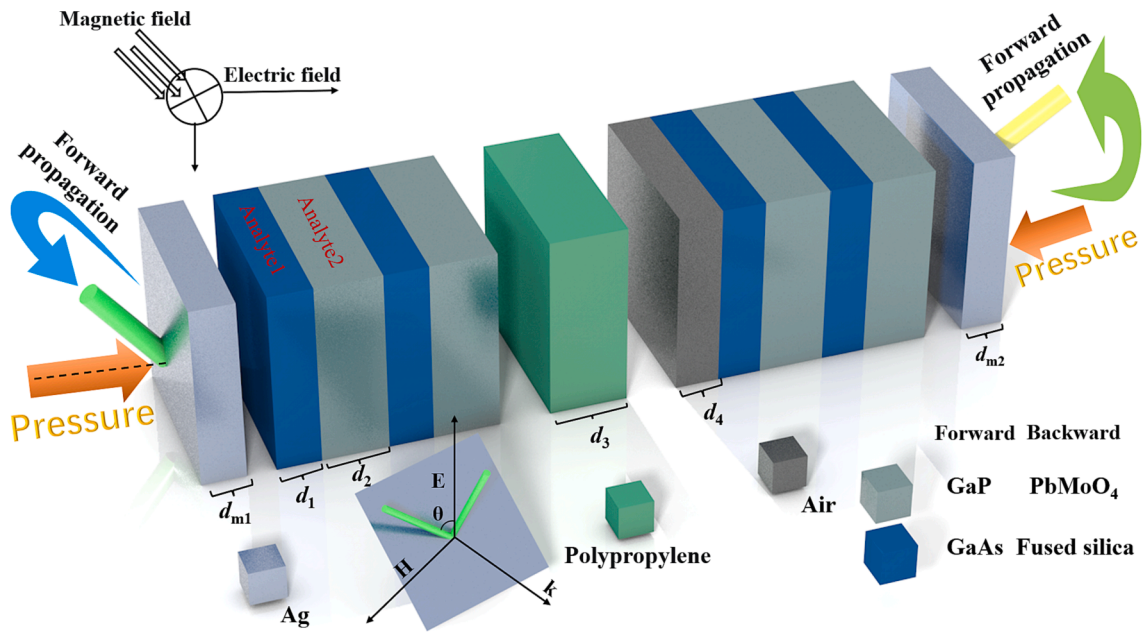


Fig. 1. The two-dimensional structure atlas of proposed Janus LPS.

one physical quantity, which reduces their practicality. In response to these challenges, the proposed LPS not only measures pressure but also incorporates the ability to measure structural deformation and incident angle. This enhancement significantly improves the sensor’s versatility. Additionally, to address the possibility of abnormal physical characteristics in extreme environments, different varistor materials are included in the design to cross-validate the measurement results and ensure measurement accuracy.

Representing the physical properties of the LPS through data poses a challenge due to its high-dimensional nature. The transfer matrix method (TMM) serves as a crucial tool for calculating the absorptivity and transmittance of EWs propagation within the LPS [17]. Conventionally, researchers manually adjust the parameters of each medium through trial and error, resulting in significant time and manpower investment. Taking inspiration from the observational and analytical practices of early humans studying animal behavior, Kennedy *et al.* proposed the particle swarm optimization (PSO) algorithm in 1995 [18]. This heuristic optimization algorithm simulates collaboration and information sharing among individuals in a flock, seeking optimal solutions to problems. Leveraging the advantages of PSO, the PSO algorithm is used to drive the TMM calculations, thereby accelerating the process and achieving results with improved attributes [19]. However, the PSO algorithm alone cannot perform high-dimensional calculations akin to TMM. By integrating the concept of matrices, the PSO algorithm is enhanced from its original two-dimensional space calculation to a four-dimensional space, expanding its applicability range and significantly facilitating research efforts.

The enhanced particle swarm optimization (EPSO) and the LPS exhibit notable advantages, enabling the formation of sharp and high-quality absorption peaks exceeding 0.9 within the working band, leveraging the characteristics of the defect film. This paper introduces a multi-material pressure sensor with Janus characteristics, employing the EPSO algorithm for optimization. The designed LPS incorporates two gaps for filling piezoresistive materials. When EWs are incident from different directions, the variation in filling piezoresistive materials results in distinct strain optical coefficients among the four materials. This significantly enhances the accuracy of pressure detection, as different materials exhibit varying changes in RI in response to a given pressure value. Consequently, the impact on the absorption rate differs, allowing for the identification and elimination of erroneous data through

comparison with other material measurements and averaging techniques, thereby greatly improving measurement accuracy. For the front incidence of EWs, the corresponding sensitivity (S), quality factor (Q) and figure of merit (FOM) values of the pressure sensor are 5.46 nm/GPa, 563.9, and 5.5 GPa⁻¹, respectively. In the case of backward incidence, the values are 10.24 nm/GPa, 316.7, and 3.3 GPa⁻¹, respectively. Furthermore, the designed LPS exhibits high S to changes in thickness, with forward-oriented S , Q , and FOM values averaging 6.64 and 4.7, 564.6 and 320.1, 6.76 nm⁻¹, and 1.47 nm⁻¹, respectively. In the forward and backward directions, the LPS can be shown the same measured pressure range, but there are differences in the working band and the quality of detection. This allows for further verification and validation of the detection results. The angle detection capability of the proposed LPS is another notable feature. It intuitively reflects changes in incident angle, offering an S value of 0.32 nm/degree, Q of 543.9, and FOM of 0.32 degree⁻¹.

In this paper, the introduction is divided into several key sections. The first part serves to elucidate the fundamental physical principles underpinning the proposed structure. The second section is dedicated to outlining the specific parameters governing the structural design. The third part expounds upon the calculation methodologies employed, with a primary focus on the TMM, EPSO, and the pertinent formulas used for evaluating sensing performance. Subsequently, the fourth section is dedicated to the comprehensive analysis and discussion of the sensor characteristics inherent to the proposed structure. Finally, the conclusion encapsulates a succinct summary of the entire manuscript. How to fabricate the given LPS can be seen Supplemental Material.

2. Theoretical model

The proposed Janus LPS consists of 12 dielectric layers arranged in a stacked configuration to form a multifunctional structure capable of pressure, thickness, and angle detection, as illustrated in Fig. 1. The designed LPS can be represented as $M_1(A_1A_2)^2KN(A_1A_2)^2M_2$. The layers M_1 and M_2 which are shown in light gray regions in Fig. 1, characterized by different thicknesses d_{m1} and d_{m2} , respectively, are positioned on both sides of the structure, and their dielectric constants are the same.

In the operating band of the device, the dielectric constant of the metallic silver (Ag) can be described as follows [20]:

$$\varepsilon_{Ag} = \varepsilon_{\infty} - \frac{\omega_p^2}{j\omega\gamma + \omega^2} - \frac{\Delta\Omega^2}{(\omega^2 - \Omega^2) + j\tau}, \quad j = \sqrt{-1}. \quad (1)$$

where $\omega = 2\pi f$ is the angular frequency and f is the frequency. $\varepsilon_{\infty} = 2.4064$ on behalf of the limiting frequency of the dielectric constant. $\omega_p = 2\pi \times 2214.6 \times 10^{12}$ Hz indicates the plasma frequency. $\gamma = 2\pi \times 2214.6 \times 10^{12}$ represents the collision frequency. $\Delta = 1.6604$ indicates the Lorentz project weight. $\Omega = 2\pi \times 1330.1 \times 10^{12}$ Hz represents the Lorentz resonance strength. $\tau = 2\pi \times 620.7 \times 10^{12}$ is the vibrational spectrum width [32]. Due to the exceptional electrical conductivity and excellent ductility of Ag, it is utilized on both sides of the structure, facilitating the design and improvement of the LPS. A_1 and A_2 correspond to analyte 1 and analyte 2 which are shown in dark blue and dark gray regions in Fig. 1. When EWs is incident from the front, A_1 is filled with gallium arsenide (GaAs) ($n_1 = 3.32$) [21], n on behalf of the RI of medium, while A_2 is filled with gallium phosphide (GaP) ($n_2 = 3.43$) [22]. In the reverse configuration, the dark blue region is filled with fused silica ($n_3 = 1.46$) [23], and the cyan region is filled with lead molybdate (PbMoO₄) ($n_4 = 2.39$) [24]. The filling materials in analyte 1 and analyte 2 serve as piezoresistive materials, with respective thicknesses d_1 and d_2 . The periodic arrangement of LPS is disrupted by the introduction of a defective film in the central region, and the entire structure exhibits symmetrical distribution around the intermediate medium. The nonlinear materials K and N are characterized by thicknesses d_3 and d_4 which are shown in palm green and coffee black in Fig. 1, respectively, representing polystyrene and air ($n_5 = 1$). Under the influence of an electric field (E), the RI of the parallel and perpendicular polarized light waves changes differently, resulting in the Kerr effect [25]. When a nonlinear defect is introduced into an ordinary medium, the dielectric constant cannot be directly obtained and requires calculation using the corresponding formula [26]:

$$E_i = \sqrt{\frac{2It}{c \times E_0}}, \quad (2)$$

where $E_0 = 8.854 \times 10^{-12}$ F/m denotes electric permittivity in a vacuum, the It on behalf of the illumination intensity, and $c = 3 \times 10^8$ m/s stands for the speed of light. And the expression of nonlinear RI is [26]:

$$n_N = n_0 + \frac{x_3 \times |E|^2}{2n_0}, \quad (3)$$

where the third-order nonlinear polarizability is represented by x_3 . In this study, the designed LPS operates in the transverse electromagnetic (TE) wave. The distinguishing feature of the TE wave is that it exhibits a magnetic field (H) component during electromagnetic wave transmission, and the direction of propagation is always perpendicular to the H . In Fig. 1, the H direction is perpendicular to the inward side of the paper, while the E direction is reversed along the EWs propagation direction. On the gray-blue medium plane, the H direction is parallel to the medium plane, and E direction is perpendicular to the medium plane, and it has a θ -deflection Angle distribution with the incident EWs. EWs in this study operate within two distinct wavelength domains, spanning 500 ~ 600 nm and 900 ~ 1100 nm. Concerning polarization direction, the electric field oscillates tangentially along the material surface in TE mode. The incidence angle is treated as a variable, and the illumination intensity is standardized at the typical sunlight intensity of 50000 lx. Additionally, no other specific polarization states are considered in this investigation. The proposed structure is composed of several dielectric layers, each with specific roles. Of utmost significance are the nonlinear defect layer and the air layer, synergistically employed in crafting the defect film to achieve a sharp and high peak absorption rate. Additionally, two analyte layers, denoted A_1 and A_2 , serve the purpose of substance placement detection. Notably, the dielectric silver layers positioned on both sides play a crucial role, particularly in the infrared spectrum, due to their exceptional optical properties. These layers

enhance sensing detection capabilities and facilitate the propagation of EWs.

3. Calculation methods

3.1. TMM

Through the derivation of Maxwell's equation [27], the relationship between the E and H in these two layers can be described by a two-row, one-column matrix multiplication. Mathematically, this relationship can be expressed as follows [28]:

$$\begin{pmatrix} E_u \\ H_u \end{pmatrix} = M \begin{pmatrix} E_{u+1} \\ H_{u+1} \end{pmatrix}. \quad (4)$$

In the TE mode, the product relation satisfying E and H between any two layers satisfies a high-dimensional matrix [28]:

$$M_u^{TE} = \begin{pmatrix} \cos(k_{uz}d_u) & -\frac{j}{\eta_u^{TE}} \sin(k_{uz}d_u) \\ -j\eta_u^{TE} \sin(k_{uz}d_u) & \cos(k_{uz}d_u) \end{pmatrix}, \quad (5)$$

where

$$k_{uz} = k_u \cos\theta, \quad (6)$$

$$k_u = \frac{\sqrt{\varepsilon_u}\omega}{c} \quad (7)$$

$$\eta_u^{TE} = \sqrt{\frac{\varepsilon_0}{\mu_0}} \sqrt{\varepsilon_u} \cos\theta_u, \quad (8)$$

where d_u and ε_u stand for the thickness and the dielectric constant of the u th layer.

According to Snell's law of refraction [28]:

$$\theta_u = \arcsin\left(\frac{n_0 \sin(\theta_0)}{n_u}\right), \quad (9)$$

where n_0 represents the RI of the medium from which the incident light originates, n_u on behalf of the RI of the medium in which the u th layer is located, and θ_0 stands for the angle of incidence as the light enters the structure from the air.

Therefore, according to the rules of matrix multiplication, when multiplying matrices of the same dimension, the resulting dimension remains unchanged. After EWs pass through the entire LPS, the calculation formula of the whole structure is expressed as:

$$M = \sum_{j=1}^U M_j = \begin{pmatrix} M_{11} & M_{12} \\ M_{21} & M_{22} \end{pmatrix}. \quad (10)$$

The TMM in the normal nodal layer differs significantly from the TMM in the nonlinear layer structure. After obtaining the E at the back interface of the entire nonlinear medium, the LPS is divided into multiple equally spaced layers. Then, starting from the back interface and moving towards the front, the nonlinear TMM equations can be derived step by step for the front and back interfaces of each layer of the nonlinear medium [29].

$$\begin{pmatrix} E_u \\ H_u \end{pmatrix} = O_1 O_2 O_3 \cdots O_m = O_D \begin{pmatrix} E_{m+1} \\ H_{m+1} \end{pmatrix}, \quad (11)$$

$$M = O_B O_D O_R, \quad (12)$$

where O_B and O_D are the transfer matrices relatively derived from the front and back interfaces of the nonlinear medium.

The equations of the coefficient of reflection (r) and coefficient of transmission (t) can be expressed as [28]:

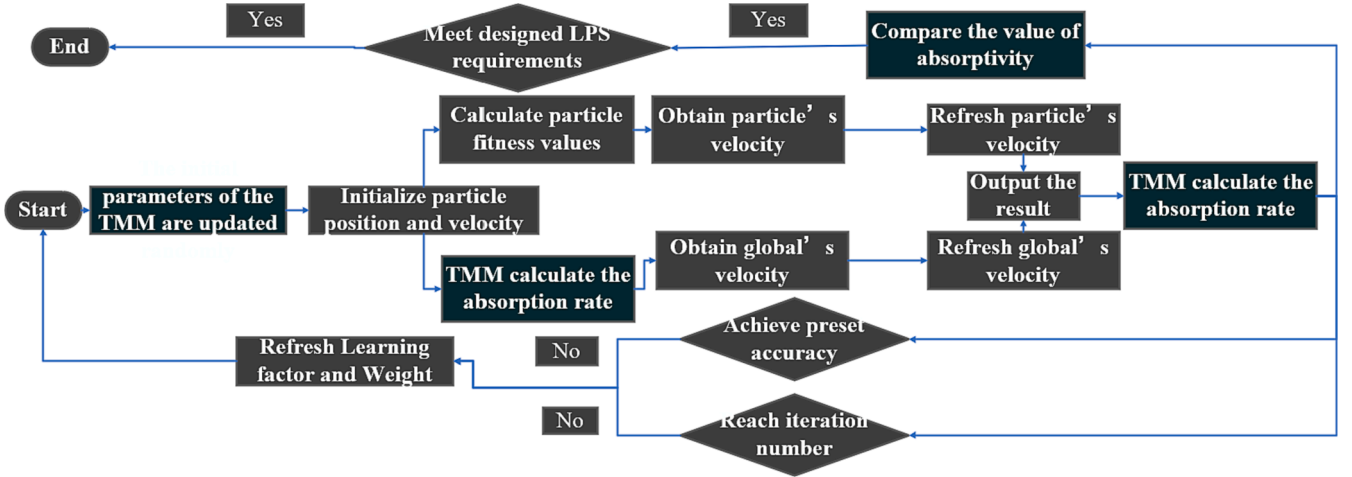


Fig. 2. The process of ESPO drives the TMM.

$$r = \frac{(M_{11} + M_{12}\eta_{U+1})\eta_0 - M_{21} - M_{22}\eta_{U+1}}{(M_{11} + M_{12}\eta_{U+1})\eta_0 + M_{21} + M_{22}\eta_{U+1}} \quad (13)$$

$$t = \frac{2\eta_0}{(M_{11} + M_{12}\eta_{U+1})\eta_0 + M_{21} + M_{22}\eta_{U+1}} \quad (14)$$

The equations for reflectance (R), transmittance (T) and absorbance (A) are described as [28]:

$$R = r \cdot r^* \quad (15)$$

$$T = t \cdot t^* \quad (16)$$

$$A = 1 - T - R \quad (17)$$

where r^* and t^* stand for the conjugate values of r and t .

3.2. EPSO

PSO is a widely employed method for solving nonlinear equations due to its superior ability to search for optimal solutions within a specified space dimension. Compared to other optimization algorithms, PSO excels in its capability to identify excellent solutions. To harness this optimization potential, the dimensionality of the calculation must be increased to w , representing the parameter variable to be optimized. Consequently, the matrix that stores the particles becomes a W -dimensional matrix. Envisioning a known space, each example's total space coordinates correspond to a constraint function. By solving these coordinates, the final result can be obtained. The iterative formula for the particle's position and velocity vector is paramount in the entire algorithm flow [30].

$$\begin{cases} X_{k+1}(w) = X_k(w) + V_k(w) \\ V_{k+1}(w+1) = iV_k(w) + \sum_{P_i \in N_k} c_i r_i (P_i(w) - X_k(w)) \end{cases} \quad (18)$$

$$w = 1, 2, \dots, W_F, k = 0, 1, 2..D$$

The parameter W_F is the number of particle swarms, while D is the number of iterations. $X(w)$ represents the position of the particle, $V(w)$ signifies the directional velocity vector, and $P(w)$ is utilized to store the optimal positions. $P(w)$ can be further divided into individual optimal positions, denoted as $P_{indi}(w)$, and collective optimal positions, represented as $P_{gro}(w)$. The subscript i represents the inertia factor, which captures the influence of the original velocity on the subsequent generation's updated velocity. On the other hand, c_i denotes the learning factor, which governs the impact of the particle's own best position and

the swarm's best position on the velocity update. To enhance the application efficiency of PSO, this paper introduces EPSO, an enhanced version of the algorithm. Building upon Eq.(18), the second-order oscillation link method is incorporated to improve the algorithm and enhance particle diversity. The specific formula is as follows [31]:

$$\begin{cases} X_k(w+1) = X_k(w) + V_k(w+1) \\ V_k(w+1) = \omega \times V_k(w) + \varphi_1(P_{indi}(w) - (1 + \xi_1)X_k(w) + \xi_1 X_k(w-1)) \\ \quad + \varphi_2(P_{gro}(w) - (1 + \xi_2)X_k(w) + \xi_2 X_k(w-1)) \end{cases}$$

$$w = 1, 2, \dots, W_F, k = 0, 1, 2..D$$

$$\varphi_1 = c_1 r_1, \varphi_2 = c_2 r_2$$

$$\xi_1 < \frac{2\sqrt{\varphi_1} - 1}{\varphi_1}, \xi_2 < \frac{2\sqrt{\varphi_2} - 1}{\varphi_2} \quad (19)$$

The variables in Eq.(19) are defined in the same manner as in Eq. (18). It is important to note that ω is a tunable constant and φ is the product of the learning factor and random parameters uniformly distributed in the interval $0 \sim 1$. EPSO incorporates the concept of oscillation, which allows for strong global search capability and oscillation convergence in the early stages of the algorithm. In the later stages, it focuses on strengthening local search and asymptotic convergence. The specific operation process of EPSO is illustrated in Fig. 2.

3.3. Sensing performance

The LPS-based sensor design employs a consistent formula for calculating performance indices, with a focus on the calculation methods of S , Q , and FOM [32]. The parameters you need to know before giving the equation. $\Delta\lambda$ and Δn represent the changes in wavelength and RI, respectively. The parameter λ_T denotes the peak wavelength, while $FWHM$ is the full width at half maximum of the absorption or transmission peak.

$$S = \frac{\Delta\lambda}{\Delta n} \quad (20)$$

$$Q = \frac{\lambda_T}{FWHM} \quad (21)$$

$$FOM = \frac{S}{FWHM} \quad (22)$$

$$LOD = \frac{f_r}{20 \cdot S \cdot Q} \quad (23)$$

Table 1
EPSO optimization parameters.

Parameter	EPSO			Parameter	Range	unit	Optimization result
	range	unit	Optimization result				
d_1	$10 \sim 10^3$	nm	39.3	x_3	$1 \sim 5 \times 10^{-12}$	C·m ² /V	1.14×10^{-12}
d_2	$10 \sim 10^3$	nm	21.5	n_4	1 ~ 5	None	1
d_3	$10 \sim 10^3$	nm	321	Forward			
d_4	$10 \sim 10^3$	nm	65.2	n_1	1 ~ 5	None	3.32
d_{m1}	$10 \sim 10^3$	nm	64.7	n_2	1 ~ 5	None	3.43
d_{m2}	$10 \sim 10^3$	nm	23.2	Backward			
θ	0 ~ 90	degree	20	n_1	1 ~ 5	None	1.46
It	$0 \sim 10^5$	lx	4000	n_2	1 ~ 5	None	2.39

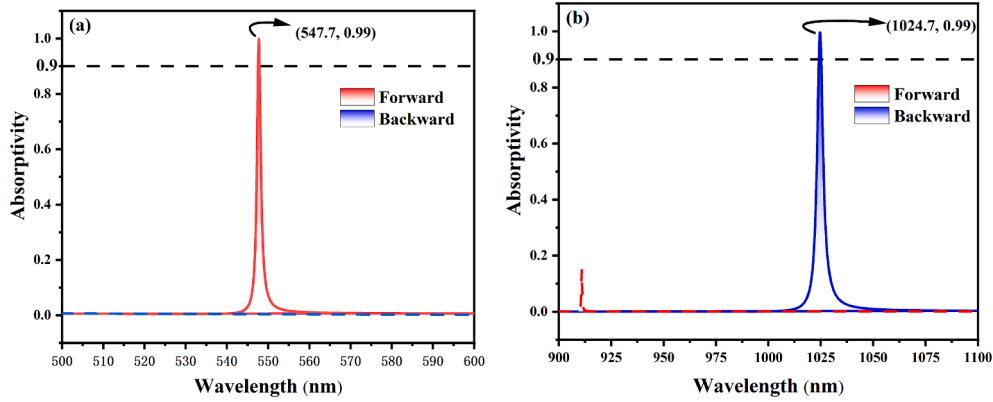


Fig. 3. The absorption peak of EWs incident from forward and backward. Operating band: (a) 500 nm ~ 600 nm, (b) 900 nm ~ 1100 nm.

$$DA = \frac{\Delta\theta_{SPR}}{FWHM} \quad (24)$$

The limit of detection (*LOD*) is a crucial parameter for assessing sensing capabilities [42]. A lower *LOD* value indicates better performance and the ability to detect even subtle changes in sensing. Here, f_T denotes the peak frequency. Detection ability (*DA*) characterizes an instrument or sensor’s capacity to identify a specific target analyte under

defined conditions [43]. *DA* is quantified as the ratio of the resonant angular displacement ($\Delta\theta_{SPR}$) to the *FWHM* of the reflection curve, and it is expressed in unitless terms.

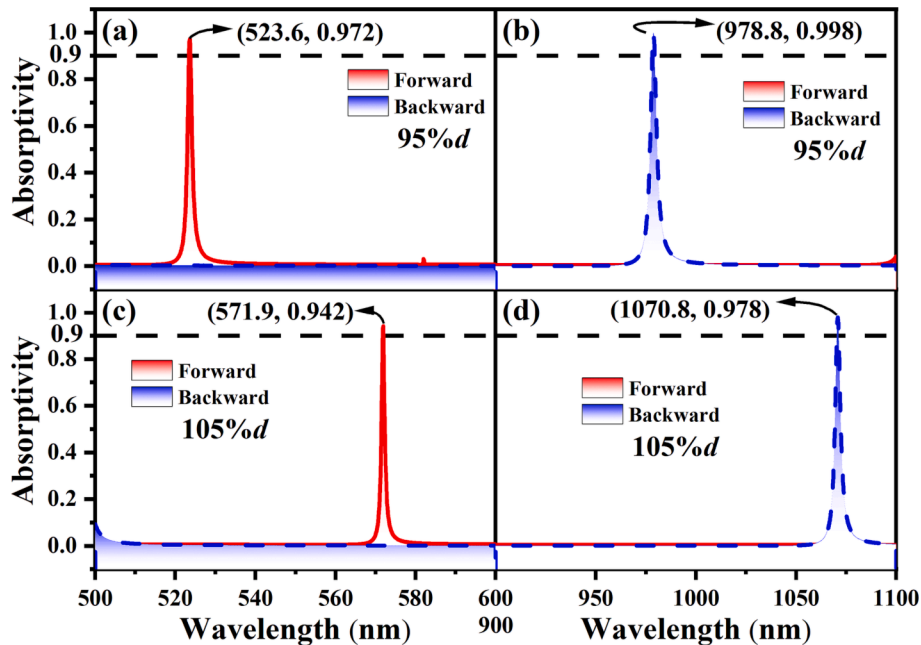


Fig. 4. Effect of fabrication tolerance on physical properties (a)95 %d, 500 ~ 600 nm, (b)95 %d, 500 ~ 600 nm, (c)105 %d, 500 ~ 600 nm, (d)105 %d, 900 ~ 1100 nm.

4. Analysis and discussion

4.1. Define structural parameters and verify feasibility

After constructing the initial LPS structure based on the conditions of the nonlinear defect mode, this study utilizes EPSO to optimize the thickness of each dielectric layer ($d_1 \sim d_4$, $d_{m1} \sim d_{m2}$), the incidence angle (θ) of the EWs, and the RIs of the analyte and medium N (n_1, n_2, n_4) within the wavelength range of 1 ~ 2000 nm which stand for the general wavelength sensor operating range. The objective is to identify specific wavelength points in the operating band where the absorptivity exceeds 0.9 and approaches 1. Utilizing the advantages of the defect mode, the design structure achieves not only a high absorption point but also a decreasing and symmetrically distributed absorption rate around the wavelength, resulting in the formation of relatively sharp absorption peaks within a specific wavelength range. The optimization results are summarized in Table 1, and further improvements were made to the basic LPS structure. In Table 1, it is important to clarify the range setting for each parameter which represents the range that conforms to the laws of physical implementation. In EPSO, the optimization range of parameters can be constrained. For the thickness parameter, values greater than 10 nm are considered feasible for practical fabrication processes, while values exceeding 1000 nm may result in a structure size that is too large for practical applications. Hence, the thickness range is set between 10 nm and 1000 nm. The RI constraint is set from 1 to 5, encompassing the typical range of refractive indices found in natural substances.

We set each parameter of thickness to $d_1 = 39.3$ nm, $d_2 = 21.5$ nm, $d_3 = 321$ nm, $d_4 = 65.2$ nm, $d_{m1} = 64.7$ nm. The parameters of RI are $n_4 = 1$, forward, $n_1 = 3.32$ and $n_2 = 3.43$, backward, $n_1 = 1.46$, and $n_2 = 2.39$. Since the RI of the analyte n_1 and n_2 depend on the material filled later, the forward and backward incidence has Janus characteristics. At the same time, the θ is adjusted to 20 degrees. The optimization results obtained through EPSO demonstrate the formation of sharp absorption peaks within the working band, as illustrated in Fig. 3. In Fig. 3(a), at a wavelength of 547.7 nm, the absorption rate exceeds 0.99. Similarly, in Fig. 3(b), when the EWs are reverse-incident, the operating frequency band shifts, but the absorption rate still maintains 0.99 at a wavelength of 1024.7 nm. Whether it is forward or reverse incidence, the proposed LPS exhibits high absorptivity and a well-defined peak shape. Furthermore, the wavelength difference at an absorptivity of 0.5 is small, indicating a narrow and pointed absorption peak. This characteristic suggests that the structure possesses favorable values of Q and FOM , making it suitable for sensor fabrication.

When considering the design of an LPS, it is essential to account for the impact of fabrication tolerances on the structural parameters. Specifically, this involves evaluating the effects of varying layer thicknesses within a range of $\pm 5\%$ of the originally specified values on the physical properties of the completed LPS. To explore this influence, each layer's thickness was set at 95% and 105% of its initially designated value. The findings are presented in Fig. 4. In Fig. 4, the red and blue curves depict the incidence of EWs from different directions. Notably, in Fig. 4(a) and 4(b), corresponding to negative tolerance, a conspicuous deviation to the right is evident in the peak curve at 95% of the designated thickness, while the curves in other measurement ranges remain smooth. A similar phenomenon persists in Fig. 4(c) and 4(d), which represent the case of 105% thickness, albeit with the curve shifting to the left as the thickness increases. In light of these observations, it can be deduced that alterations in overall thickness unavoidably led to the appearance of sharp curves. However, it's noteworthy that such changes primarily affect the frequency point while leaving the fundamental physical properties of the structure unaltered. Consequently, it can be affirmed that production tolerances exert only a modest influence on the proposed structure.

To validate the working principle of the proposed LPS and ensure that the design meets the requirements of the defect film, a simulation calculation of the E distribution is conducted in the overall structure, as

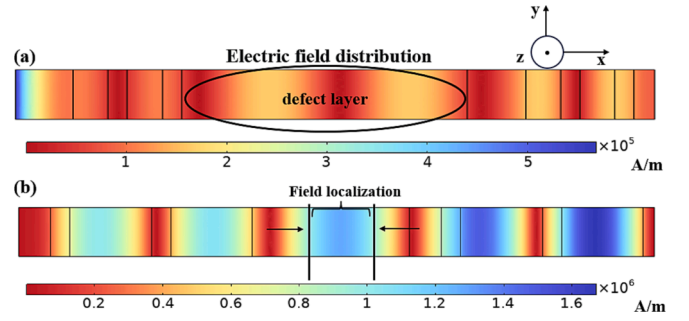


Fig. 5. E distribution of proposed LPS. (a) Forward. (b) Backward.

depicted in Fig. 5. In Fig. 5(a), the observation is revealed that apart from the higher E value on the left side, the distribution is predominantly dark blue, with the rest of the E values generally low, forming intervals of high and low values, indicated by dark red and red-orange regions, respectively. Notably, the E assumes a higher magnitude at the location of the defective film in the middle, thereby breaking the conventional periodic arrangement. Similarly, in the case of backward incidence shown in Fig. 5(b), a more pronounced distribution is observed. The E is prominently distributed at the nonlinear defect location, as well as in the subsequent arrangement of analytes A_1 and A_2 , where the E is localized in the middle of the medium because the E at this position is obviously larger than that on both sides of the medium. The obtained E distribution aligns with the design expectations, thereby establishing a solid foundation and providing the necessary conditions for sensing based on the proposed LPS.

4.2. Forward sensing function

4.2.1. Angle sensing

First, it is important to highlight the unique properties of forward incident EWs. By adjusting the incidence angle from 0 degrees to 20 degrees, 40 degrees, 50 degrees, and 59 degrees, the corresponding peak wavelength also shifts from 550.6 nm to 532.2 nm. As the Angle increases, the value of the absorption peak gradually decreases, ranging from 0.999 to 0.998, 0.970, and 0.954. At an incident Angle of 59 degrees, the value reaches 0.901, which is still above the threshold of 0.9. From the overall image, it exhibits a trend of moving toward the lower left. Throughout the working band, the absorption rate can be maintained above 0.9, and there are no other peaks with absorptivity greater than 0.1, ensuring interference-free operation during angle sensing, as depicted in Fig. 6(a). To demonstrate the wavelength shift phenomenon across the entire range with angle adjustment, a two-dimensional space with the horizontal coordinate is proposed to stand for the angle, and the vertical coordinate representing the wavelength. Color was added to represent the absorptivity, and the resulting x-y change curve approximates a straight line, as shown in Fig. 6(b). The transition from orange to bright red color represents a change in absorptivity from 0.8 to 1. Additionally, a noticeable red bending curve can be observed in the figure, indicating that the shift in Angle does not follow the same pace as the crest wavelength over the Angle change range of 0 to 59 degrees. The appearance of the red area extends on both sides as a transition from color to dark blue, indicating that the absorption rate gradually decreases from above 0.9 to 0, forming a continuous process from 1 to 0. Furthermore, to verify the correlation between the wavelength and the angle, we extracted the transverse and longitudinal values corresponding to the peaks in Fig. 6(a) and plotted their relationship curve, as illustrated in Fig. 6(c). The angle exhibits a strong linear relationship with the corresponding working wavelength, with a correlation coefficient of up to 0.982 and an S value of up to 0.32 nm/degree. The fitting equation between them can be expressed as

$$f = -0.32\theta + 552.157. \quad (25)$$

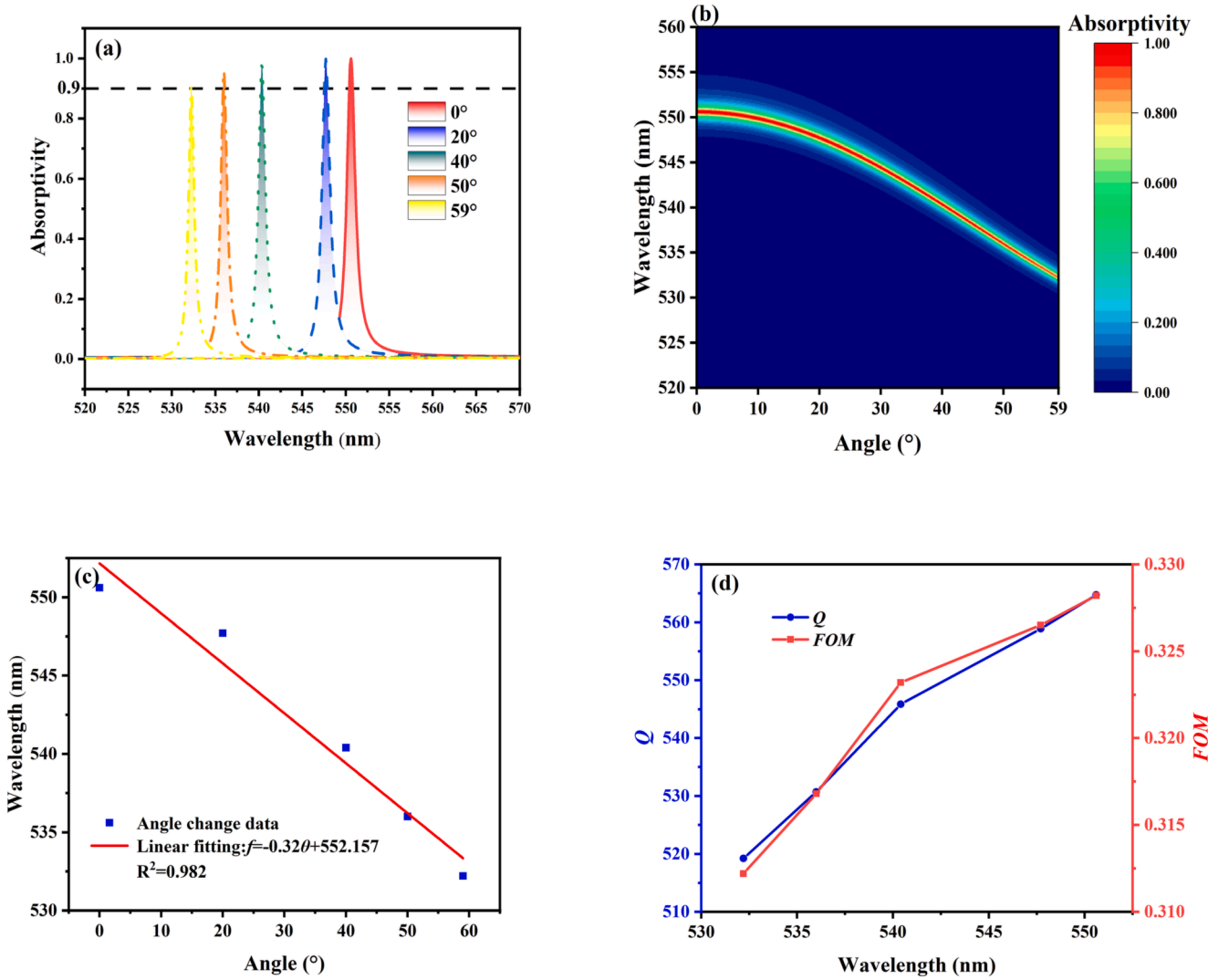


Fig. 6. (a) Shift pattern of absorption peak with incident angle. (b) Two-dimensional heat map of angle, operating wavelength and absorptivity. (c) Linear relationship between incidence angle and peak frequency point. (d) The Q and FOM of sensing performance.

Thus, it can be concluded that this is a standard wavelength-modulated angle sensor. To further emphasize the superiority of this angle sensor, we employed Eqs.(21) and (22) to calculate the sensing performance and graphically display the resulting Q and FOM values, as shown in Fig. 6(d). The overall growth trend of Q and FOM is not consistent, and the growth rate of Q and FOM from 532.2 nm to 540.4 nm is slightly higher than that from 540.4 nm to 550.6 nm. It can be observed that the overall Q and FOM values exhibit an increasing trend with the size of the operating wavelength, which is directly related to the curve becoming shorter and wider as the wave crest shifts to the left in Fig. 5(a). After data processing, the maximum Q and FOM values reached 564.7 and 0.328 degree⁻¹, respectively, while the minimum values remained above 519.2 and 0.312 degree⁻¹. The standard deviation was only 19 and 0.006 degree⁻¹. The surface angle sensing maintained a relatively stable state across the entire working band.

4.2.2. Pressure sensing

The main highlight of the designed LPS is its capability to detect pressure, which exhibits a favorable performance for both forward and backward incident EWs. The working principle is based on the fact that external pressure affects the refractive index of the pressure-sensitive material, consequently influencing the absorption rate of propagating EWs within the designed LPS. In the case of piezoresistive materials, the

relationship between applied pressure and RI can be described using tensor notation, incorporating the photo-elastic effect and stress-dependent force relationship [33]:

$$\Delta\left(\frac{1}{n^2}\right) = \sum p_{ij}\sigma_j, \quad (26)$$

where n is RI of piezoresistive material, p_{ij} , and σ_j are strain optical coefficient and stress component, respectively. The strain optical coefficient is a crucial parameter that characterizes the relationship between strain and birefringence in a material. Birefringence refers to the property of a material where light passing through it splits into two beams with different polarization states. When a material undergoes mechanical stress or strain, its RI changes, which directly affects its birefringence. The strain optical coefficient, typically denoted as p_{11} , p_{12} , p_{44} , etc., quantifies the magnitude of this effect. These coefficients are material-specific and depend on factors such as the crystal structure and mechanical properties of the material. Understanding and utilizing strain optical coefficients is essential for the design and utilization of photo-elastic materials. Photo-elastic materials enable the study of stress distribution in solids by analyzing changes in light polarization when the material is subjected to stress.

In everyday scenarios, the center of gravity of two interacting objects may not necessarily align, and forces may not act uniformly on a surface.

Table 2
The photo-elastic constants of used materials [35].

Material	n_0	p_{11}	p_{12}	C_1 ($10^{-12}/\text{Pa}$)	C_2 ($10^{-12}/\text{Pa}$)
GaAs	3.43	-0.165	-0.140	-18.39	-10.63
Fused silica	1.46	0.121	0.270	0.65	4.50
GaP	3.32	-0.151	-0.082	-17.91	-1.87
PbMoO ₄	2.39	0.24	0.24	6.63	6.63

Table 3
RI of forward pressure resistance materials [35].

External pressure (GPa)	0	1	2	3	4	5
GaAs	3.43	3.4685	3.5069	3.5454	3.5838	3.6223
GaP	3.32	3.3417	3.3633	3.3849	3.4066	3.4282

Therefore, for the purpose of this study, the force considered only accounts for the pressure applied perpendicular is assumed to the structural plane, and that the pressure exerted on the LPS structure is uniformly distributed across the surface. The specific pressure direction is depicted by the orange shear head in Fig. 1, acting vertically at the center of the surface of the Wolf gray medium. The relationship between external pressure and RI can be modified as [34–35]:

$$n = n_0 - (c_1 + c_2)\sigma, \quad (27)$$

where c_1 and c_2 are functions closely related to the strain optical coefficient,

$$c_1 = \frac{n_0^3(p_{11} - 2Vp_{12})}{2E}, \quad (28)$$

$$c_2 = \frac{n_0^3(p_{11} - 2V(p_{11} - p_{12}))}{2E}. \quad (29)$$

In the modified relationship, n_0 represents the RI of the material at zero pressure. The parameters p_{11} and p_{12} correspond to the strain

optical coefficient, which describes the change in RI with applied pressure. E represents the material’s Young’s modulus, which characterizes its stiffness, and V denotes Poisson’s ratio, which describes the material’s lateral contraction in response to axial strain. Table 2 provides the photo-elastic constants for several used materials, which are essential for studying and understanding the configuration of piezoresistive materials in the designed LPS [35]. These photo-elastic constants describe the relationship between the applied pressure and the resulting change in RI for each material.

The given LPS is capable of detecting applied pressure regardless of the direction of incidence EWs. Specifically, when the EW is incident from the front at an angle of 20 degrees, and the layer to be measured (d_2) has a thickness of 31.5 nm, GaAs and Gap are filled at analyte 1 and analyte 2, respectively. By utilizing the strain optical coefficients provided in Table 2, Eq.(27) is applied to calculate the corresponding changes in the RI of the material under pressure ranging from 0 to 5 GPa. The calculated values are presented in Table 3.

Fig. 7(a) demonstrates that as the applied pressure increases from 0 to 5 GPa, the corresponding peak wavelength shifts towards longer wavelengths, ranging from 547.7 nm to 575 nm. The absorption rate corresponding to 0 GPa is as high as 0.999. With the increase of applied pressure, the peak absorption rate remains at 0.998 for 1 GPa, 0.995 for 2 GPa, and stays near 0.990 for pressures from 3 GPa to 5 GPa. The absorption rate greater than 99 % throughout the entire range indicates the high absorption characteristics of the defective film in the proposed LPS. The overall shape of the absorption curve remains consistent, indicating a stable performance of pressure sensing. To visualize the absorbance data, a heat map is generated in Fig. 7(b), where regions with absorbance greater than 0.99 are represented in dark red, while the remaining areas are displayed in dark blue. In the whole image, the distribution of the deep red curve forms a thin line. When compared with the dark blue areas with 0 absorption rate, the range of red and orange regions with an absorption rate greater than 0.8 accounts for only about 1 % of the former. This indicates that the peak value of the absorption curve is narrow, and the ratio of bright colors (indicating high absorption) to dark blue (indicating low absorption) in the entire

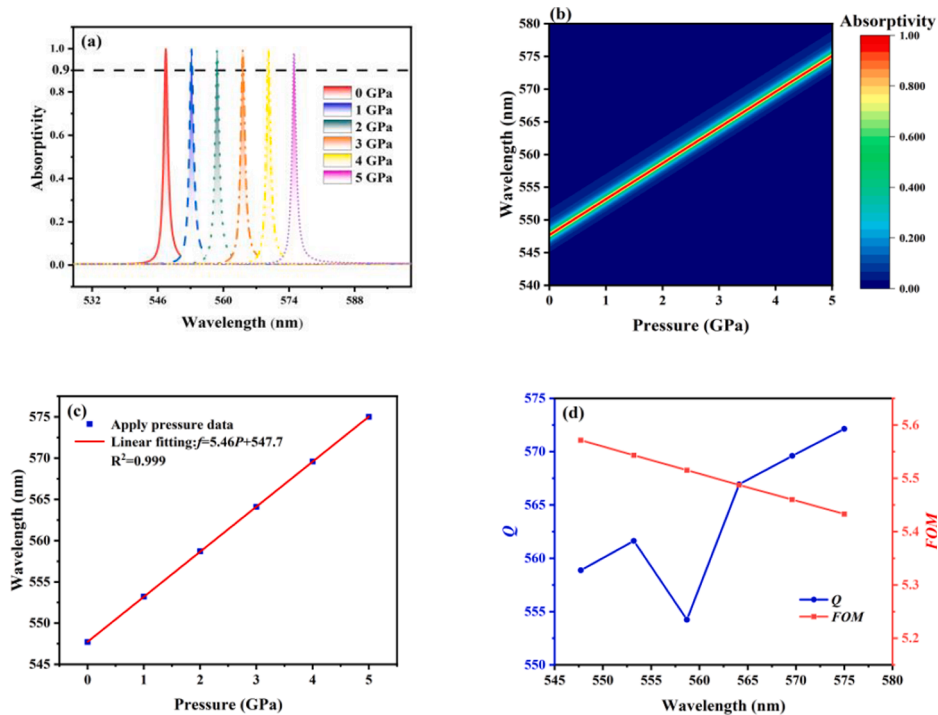


Fig. 7. (a) Curve of structural absorptivity under external pressure. (b) Full working wavelength absorption characteristics at different external pressure. (c) Linear fitting over the pressure to be measured. (d) Q and FOM curves of pressure sensing characteristics.

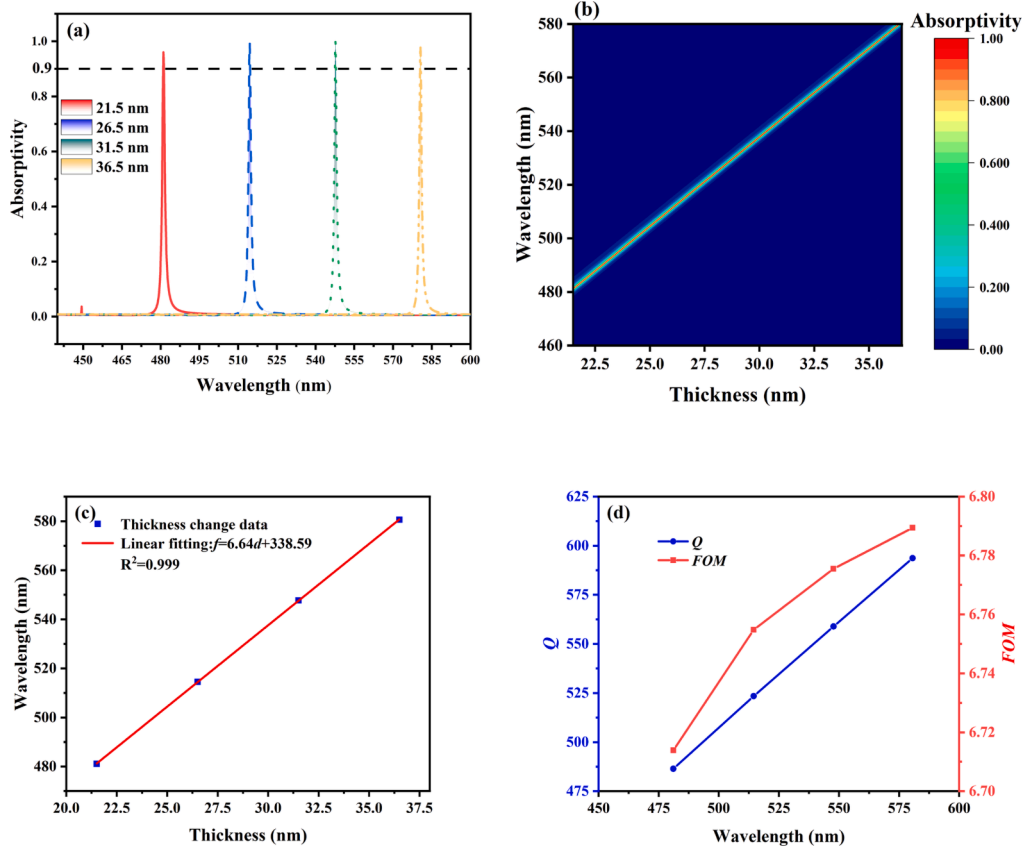


Fig. 8. (a) Absorption peaks of each wavelength point under different thickness. (b) The distribution of absorptivity in two-dimensional plots of thickness and operating wavelength. (c) Linear relationship between Peak operating wavelength and range of deformation degree. (d) Variation of Q and FOM in thickness measuring range.

region changes slightly. This observation suggests that the absorption curve remains relatively unchanged over the measured range. This heat map confirms that high absorptance exists within the entire working and pressure measurement range, ensuring reliable pressure detection without interference from low absorptance regions. Combine Fig. 7(c) the peak data by drawing, 0 GPa, 547.7 nm, 1 GPa, 553.2 nm, 2 GPa, 558.7 nm, 3 GPa, 564.1 nm, 4 GPa, 569.6 nm, 5 GPa, 575 nm. Fig. 6(c) illustrates a strong positive linear correlation between applied pressure and peak working wavelength, with a high correlation coefficient ($R^2 = 0.999$). The calculated S of the sensor is 5.46 nm/GPa, indicating its high responsiveness to changes in applied pressure. The linear fitting equation for this correlation is provided.

$$f = 5.46P + 547.7. \quad (30)$$

$S = 5.46$ nm/GPa obtained by Eq.(30), then Fig. 6(a) reads the $FWHM$ under different pressures. Through accurate calculation and analysis, Fig. 7(d) displays the Q factor of 564 and the FOM of 5.5 GPa^{-1} . Within the measured range, the maximum Q value reaches 572.1, while the minimum FOM value is 5.43 under an applied pressure of 5 GPa. The FOM exhibits a stable growth trend as the peak wavelength transitions from 547.7 nm to 575 nm. However, the Q value experiences a sudden decline from 558.7 nm to 554.24 nm, which represents the minimum value of Q . Overall, the standard deviations of Q and FOM are relatively small, with values of 6.83 and 0.05 GPa^{-1} , respectively. This indicates that the performance of the pressure sensor remains consistent and stable during the forward propagation of EWs. The small standard deviations suggest that the sensor's measurements of pressure are reliable and exhibit minimal variability. This stability is crucial for ensuring accurate and consistent pressure detection in practical applications.

4.2.3. Thickness sensing

Analyte 2, represented by the thickness d_2 , plays a crucial role in thickness detection. When external forces are applied to an object, the medium undergoes deformation, which becomes more pronounced with increasing external pressure. The designed LPS structure can detect and measure the degree of deformation specifically in analyte 2. Fig. 8(a) illustrates the presence of high absorptivity when the thickness is set at 21.5 nm and 36.5 nm, and this phenomenon is maintained at 26.5 nm and 31.5 nm as well. Since deformation caused by pressure is a continuous process, it is important to explore the impact of continuous thickness changes on the peak working wavelength and absorption rate. As the thickness is adjusted to 36.5 nm, 31.5 nm, 26.5 nm, and 21.5 nm, the corresponding absorption peak wavelengths are 580.6 nm, 547.7 nm, 514.5 nm, and 481.1 nm, respectively. The overall trend indicates that as the thickness increases, the peak shifts to the right. The absorptivity values from right to left are 96.0 %, 99.3 %, 99.8 %, and 98.3 %, respectively, showing a trend of first increasing and then decreasing. Fig. 8(b) shows the results of this exploration. The dark red areas represent high absorption rates and are distributed in a thin straight line in the figure, indicating good sensitivity. The range of absorption greater than 20 % accounts for less than 0.5 % of the entire operating band range (120 nm). In Fig. 8(c), the coordinates of the peak points are extracted for linear fitting, resulting in Eq.(31) provided. The linear relationship with an S value of 6.64 and a high correlation coefficient ($R^2 = 0.999$) confirms the functional relationship between the operating wavelength and the degree of deformation in analyte 2.

$$f = 6.64d + 338.59. \quad (31)$$

Fig. 8(d) evaluates the performance of thickness detection by examining the values of Q and FOM . As the operating wavelength shifts

Table 4
RI of backward pressure resistance materials [35].

External pressure (GPa)	0	1	2	3	4	5
Fused silica	1.46	1.4504	1.4407	1.4310	1.4214	1.4118
GaP	2.39	2.3701	2.3502	2.3303	2.3104	2.2906

towards longer wavelengths, the Q and FOM values exhibit an upward trend. At 480 nm, the Q and FOM values are 486.5 and 6.7 nm^{-1} , respectively. Eventually, with the rightward shift of the operating wavelength, the Q and FOM values reach 593.7 and 6.79 nm^{-1} , respectively. When these data are synthesized, the resulting values are 2162.4 for Q and 27 nm^{-1} for FOM . In the entire working band, the growth rate of the Q value remains relatively constant, showing a changing trend that is close to a straight line. On the other hand, the changing trend of the FOM is slightly different. Initially, there is a higher slope, indicating a higher growth rate, but as the wavelength increases, the slope decreases, and the growth rate gradually slows down.

4.3. Backward sensing function

4.3.1. Thickness sensing

It is noteworthy that the designed LPS incorporates two distinct pressure-sensitive materials, exhibiting different strain optical coefficients for forward and backward pressure sensing. This unique design enables mutual validation during pressure detection, leading to more accurate results. To enable the proper functioning of the backward pressure detection function, the analyte was refilled using Fused silica and PbMoO_4 at analytes 1 and 2, respectively, within a different working band. The variations in their RIs with pressure are presented in Table 4.

The absorption curves corresponding to six parameter points, evenly spaced from 0 GPa to 5 GPa, are depicted in Fig. 9(a). Absorption rates exceeding 0.99 are achieved at the operating wavelengths of 973.7 nm,

983.5 nm, 993.9 nm, 1004.2 nm, 1014.3 nm, and 1024.7 nm, and the corresponding absorption rate is 99.7 %,99.9 %,99.9 %,99.8 %, and 99.6 %. Within the working band, apart from the required peak values for sensing measurements, no absorption rates exceed 0.1, ensuring the stability of the system. Fig. 9(b) presents a color-coded visualization of the absorption rate distribution across the entire working band, the transition color region from deep red to bright red in the figure represents the range of absorption values from 0 % to 100 %, respectively. The deeper the red color, the higher the absorption rate, and as the color transitions to a brighter red, the absorption rate decreases, eventually reaching 0 % absorption represented by dark blue. This color gradient reflects the continuous change in the absorption rate across the entire working band and pressure range. In the operating wavelength range of 960 nm to 1040 nm, as the pressure increases from 0 GPa to 5 GPa, a noticeable trend is observed in the figure. The bright colors, represented by sky blue, olive green, orange, and vermilion, gradually shift downwards. Specifically, at 0 GPa, the peak wavelength ranges from 1020 nm to 1030 nm, while at 5GPa, the peak wavelength shifts to the range of 970 nm to 980 nm. Fig. 9(c) displays the linear fitting equations for pressure and operating wavelength:

$$f = -10.24P + 1024.6. \tag{32}$$

These results demonstrate an S value of up to 10.24 nm/GPa and a correlation coefficient of 0.999, indicating a linear negative correlation between the independent variable on the xy-axis and the dependent variable. $S = 10.24 \text{ nm/GPa}$. The $FWHM$, obtained as 3.1 nm from Fig. 9 (a), is utilized to calculate the sensing performance parameters using formulas 21 and 22. Fig. 9(d) showcases the mean values of Q and FOM , which are 316.6 and 3.246 nm^{-1} , respectively. The overall Q exhibits a gradually increasing trend, while FOM displays the opposite pattern. The Q value shows a slow growth rate in the wavelength range of 973.7 nm to 983.5 nm, with a minor change from 314.1 to 314.2. However, in the range of 983.5 nm to 1024.6 nm, the Q value experiences a

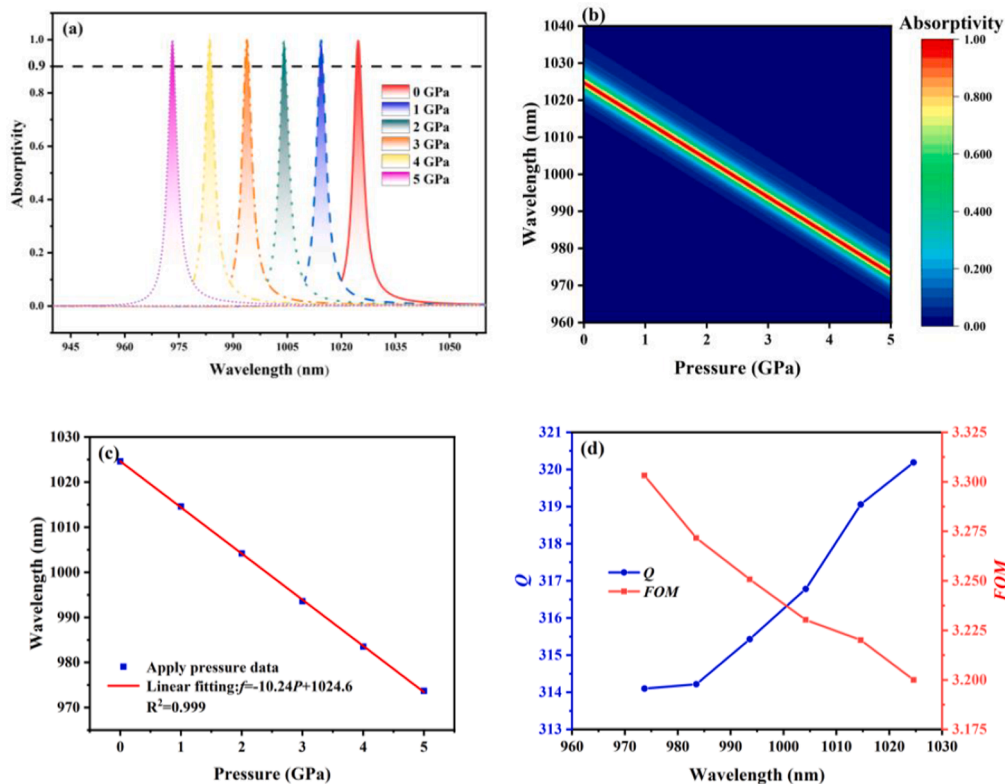


Fig. 9. (a) The movement of absorption peak under different pressure point. (b) The distribution of absorptivity over the entire operating band and measuring range. (c) Curve relationship between pressure and peak wavelength point. (d) FOM and Q values at different external pressure.

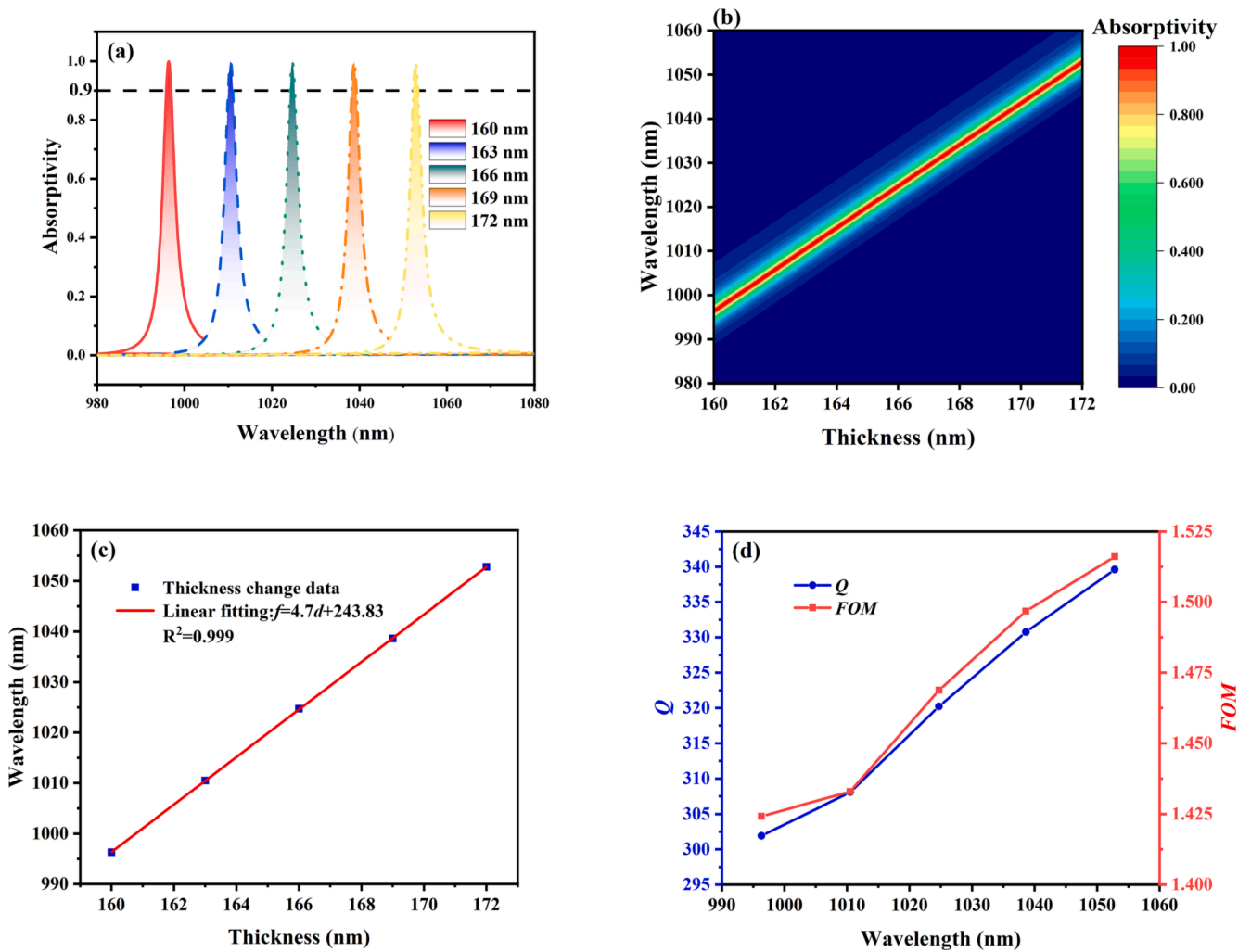


Fig. 10. (a) Absorptivity characteristics of different cavity thicknesses at different wavelength points. (b) Full wavelength absorptivity characteristics at different thicknesses. (c) Linear fitting over the thickness to be measured. (d) Sensing performance over a range of thickness variations.

substantial increase from 312.4 to 320.2, indicating a significant improvement in sensor performance. On the other hand, the decrease rate of FOM remains relatively stable, with a slowdown observed in the wavelength range of 1004.2 nm to 1014.6 nm. These findings highlight the sensitivity of the LPS sensor to different operating wavelengths, enabling precise and tailored measurements across the working band. The calculated standard deviations are 2.54 and 0.037 nm^{-1} , signifying weak variations in the sizes of Q and FOM and consistent relative quality during the measurements.

4.3.2. Thickness sensing

The cavity position for thickness measurement remains constant, but the measurement range has shifted from 160 nm to 172 nm. Within this subrange, the corresponding peak operating wavelengths range from 996.3 nm to 1053 nm, as depicted in Fig. 10(a). Throughout the entire working band range, the peak absorption rate of the curve remains consistently above 0.9, which serves as a solid foundation for the sensor's preparation. As the wavelength shifts from 996.3 nm to 1053 nm, the corresponding absorption rates are 99.9 %, 99.8 %, 99.6 %, 98.7 %, 98.5 %, 98.3 %, 98.1 %, 97.9 %, 97.7 %, 97.5 %, 97.3 %, 97.1 %, 96.9 %, 96.7 %, 96.5 %, 96.3 %, 96.1 %, 95.9 %, 95.7 %, 95.5 %, 95.3 %, 95.1 %, 94.9 %, 94.7 %, 94.5 %, 94.3 %, 94.1 %, 93.9 %, 93.7 %, 93.5 %, 93.3 %, 93.1 %, 92.9 %, 92.7 %, 92.5 %, 92.3 %, 92.1 %, 91.9 %, 91.7 %, 91.5 %, 91.3 %, 91.1 %, 90.9 %, 90.7 %, 90.5 %, 90.3 %, 90.1 %, 89.9 %, 89.7 %, 89.5 %, 89.3 %, 89.1 %, 88.9 %, 88.7 %, 88.5 %, 88.3 %, 88.1 %, 87.9 %, 87.7 %, 87.5 %, 87.3 %, 87.1 %, 86.9 %, 86.7 %, 86.5 %, 86.3 %, 86.1 %, 85.9 %, 85.7 %, 85.5 %, 85.3 %, 85.1 %, 84.9 %, 84.7 %, 84.5 %, 84.3 %, 84.1 %, 83.9 %, 83.7 %, 83.5 %, 83.3 %, 83.1 %, 82.9 %, 82.7 %, 82.5 %, 82.3 %, 82.1 %, 81.9 %, 81.7 %, 81.5 %, 81.3 %, 81.1 %, 80.9 %, 80.7 %, 80.5 %, 80.3 %, 80.1 %, 79.9 %, 79.7 %, 79.5 %, 79.3 %, 79.1 %, 78.9 %, 78.7 %, 78.5 %, 78.3 %, 78.1 %, 77.9 %, 77.7 %, 77.5 %, 77.3 %, 77.1 %, 76.9 %, 76.7 %, 76.5 %, 76.3 %, 76.1 %, 75.9 %, 75.7 %, 75.5 %, 75.3 %, 75.1 %, 74.9 %, 74.7 %, 74.5 %, 74.3 %, 74.1 %, 73.9 %, 73.7 %, 73.5 %, 73.3 %, 73.1 %, 72.9 %, 72.7 %, 72.5 %, 72.3 %, 72.1 %, 71.9 %, 71.7 %, 71.5 %, 71.3 %, 71.1 %, 70.9 %, 70.7 %, 70.5 %, 70.3 %, 70.1 %, 69.9 %, 69.7 %, 69.5 %, 69.3 %, 69.1 %, 68.9 %, 68.7 %, 68.5 %, 68.3 %, 68.1 %, 67.9 %, 67.7 %, 67.5 %, 67.3 %, 67.1 %, 66.9 %, 66.7 %, 66.5 %, 66.3 %, 66.1 %, 65.9 %, 65.7 %, 65.5 %, 65.3 %, 65.1 %, 64.9 %, 64.7 %, 64.5 %, 64.3 %, 64.1 %, 63.9 %, 63.7 %, 63.5 %, 63.3 %, 63.1 %, 62.9 %, 62.7 %, 62.5 %, 62.3 %, 62.1 %, 61.9 %, 61.7 %, 61.5 %, 61.3 %, 61.1 %, 60.9 %, 60.7 %, 60.5 %, 60.3 %, 60.1 %, 59.9 %, 59.7 %, 59.5 %, 59.3 %, 59.1 %, 58.9 %, 58.7 %, 58.5 %, 58.3 %, 58.1 %, 57.9 %, 57.7 %, 57.5 %, 57.3 %, 57.1 %, 56.9 %, 56.7 %, 56.5 %, 56.3 %, 56.1 %, 55.9 %, 55.7 %, 55.5 %, 55.3 %, 55.1 %, 54.9 %, 54.7 %, 54.5 %, 54.3 %, 54.1 %, 53.9 %, 53.7 %, 53.5 %, 53.3 %, 53.1 %, 52.9 %, 52.7 %, 52.5 %, 52.3 %, 52.1 %, 51.9 %, 51.7 %, 51.5 %, 51.3 %, 51.1 %, 50.9 %, 50.7 %, 50.5 %, 50.3 %, 50.1 %, 49.9 %, 49.7 %, 49.5 %, 49.3 %, 49.1 %, 48.9 %, 48.7 %, 48.5 %, 48.3 %, 48.1 %, 47.9 %, 47.7 %, 47.5 %, 47.3 %, 47.1 %, 46.9 %, 46.7 %, 46.5 %, 46.3 %, 46.1 %, 45.9 %, 45.7 %, 45.5 %, 45.3 %, 45.1 %, 44.9 %, 44.7 %, 44.5 %, 44.3 %, 44.1 %, 43.9 %, 43.7 %, 43.5 %, 43.3 %, 43.1 %, 42.9 %, 42.7 %, 42.5 %, 42.3 %, 42.1 %, 41.9 %, 41.7 %, 41.5 %, 41.3 %, 41.1 %, 40.9 %, 40.7 %, 40.5 %, 40.3 %, 40.1 %, 39.9 %, 39.7 %, 39.5 %, 39.3 %, 39.1 %, 38.9 %, 38.7 %, 38.5 %, 38.3 %, 38.1 %, 37.9 %, 37.7 %, 37.5 %, 37.3 %, 37.1 %, 36.9 %, 36.7 %, 36.5 %, 36.3 %, 36.1 %, 35.9 %, 35.7 %, 35.5 %, 35.3 %, 35.1 %, 34.9 %, 34.7 %, 34.5 %, 34.3 %, 34.1 %, 33.9 %, 33.7 %, 33.5 %, 33.3 %, 33.1 %, 32.9 %, 32.7 %, 32.5 %, 32.3 %, 32.1 %, 31.9 %, 31.7 %, 31.5 %, 31.3 %, 31.1 %, 30.9 %, 30.7 %, 30.5 %, 30.3 %, 30.1 %, 29.9 %, 29.7 %, 29.5 %, 29.3 %, 29.1 %, 28.9 %, 28.7 %, 28.5 %, 28.3 %, 28.1 %, 27.9 %, 27.7 %, 27.5 %, 27.3 %, 27.1 %, 26.9 %, 26.7 %, 26.5 %, 26.3 %, 26.1 %, 25.9 %, 25.7 %, 25.5 %, 25.3 %, 25.1 %, 24.9 %, 24.7 %, 24.5 %, 24.3 %, 24.1 %, 23.9 %, 23.7 %, 23.5 %, 23.3 %, 23.1 %, 22.9 %, 22.7 %, 22.5 %, 22.3 %, 22.1 %, 21.9 %, 21.7 %, 21.5 %, 21.3 %, 21.1 %, 20.9 %, 20.7 %, 20.5 %, 20.3 %, 20.1 %, 19.9 %, 19.7 %, 19.5 %, 19.3 %, 19.1 %, 18.9 %, 18.7 %, 18.5 %, 18.3 %, 18.1 %, 17.9 %, 17.7 %, 17.5 %, 17.3 %, 17.1 %, 16.9 %, 16.7 %, 16.5 %, 16.3 %, 16.1 %, 15.9 %, 15.7 %, 15.5 %, 15.3 %, 15.1 %, 14.9 %, 14.7 %, 14.5 %, 14.3 %, 14.1 %, 13.9 %, 13.7 %, 13.5 %, 13.3 %, 13.1 %, 12.9 %, 12.7 %, 12.5 %, 12.3 %, 12.1 %, 11.9 %, 11.7 %, 11.5 %, 11.3 %, 11.1 %, 10.9 %, 10.7 %, 10.5 %, 10.3 %, 10.1 %, 9.9 %, 9.7 %, 9.5 %, 9.3 %, 9.1 %, 8.9 %, 8.7 %, 8.5 %, 8.3 %, 8.1 %, 7.9 %, 7.7 %, 7.5 %, 7.3 %, 7.1 %, 6.9 %, 6.7 %, 6.5 %, 6.3 %, 6.1 %, 5.9 %, 5.7 %, 5.5 %, 5.3 %, 5.1 %, 4.9 %, 4.7 %, 4.5 %, 4.3 %, 4.1 %, 3.9 %, 3.7 %, 3.5 %, 3.3 %, 3.1 %, 2.9 %, 2.7 %, 2.5 %, 2.3 %, 2.1 %, 1.9 %, 1.7 %, 1.5 %, 1.3 %, 1.1 %, 0.9 %, 0.7 %, 0.5 %, 0.3 %, 0.1 %.

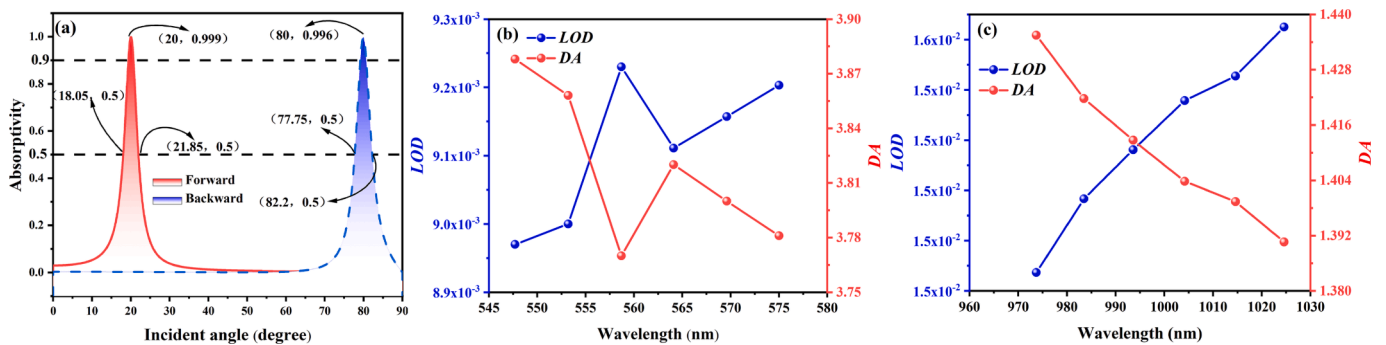


Fig. 11. (a) The frequency shift of the absorption peak under the change of incidence angle. (b) LOD and DA values for forward pressure measurements. (c) LOD and DA values for backward pressure measurements.

Table 5

The performance of published literatures compared with this work.

Refs.	Janus	Multi-physical quantity measurement	Analyte	Sensing performance		
				S	Q	FOM
This work	Forward	Yes	Pressure	5.46 nm/GPa	563.9	5.5 GPa ⁻¹
	Backward		Thickness	6.64	540.6	6.67 nm ⁻¹
			Angle	0.32 nm/degree	543.9	0.32 degree ⁻¹
			Pressure	10.24 nm/GPa	316.7	3.3 GPa ⁻¹
			Thickness	4.7	320.1	1.47 nm ⁻¹
[36]	×	×	Pressure	10.7 nm/GPa	239.53	None
[37]	×	×	Pressure	1.674 nm/GPa	228.23	0.2455
[38]	×	×	Thickness	6.67	35.53	0.418 nm ⁻¹
[39]	×	×	Pressure	0.35 nm /°C	None	0.08 K ⁻¹
[40]	×	×	Plasmonic	0.95	26.48	68
[41]	×	×	Thickness	5	40	None

and 99.1 %, respectively. Fig. 10(b) presents a three-dimensional heat map illustrating the peak wavelength, thickness, and absorptivity, visually demonstrating the feasibility of using the proposed LPS for thickness sensing. Absorptivity greater than 0.9 is observed between 160 nm and 172 nm. By extracting the peak data points from Fig. 10(a) and analyzing their linear relationship, we obtain an S value of 4.7, with the linear fitting equation expressed as follows:

$$f = 4.7d + 243.83. \quad (33)$$

This positive correlation observed in the fitting equation also affects the values of Q and FOM , leading to a progressive increase. The changing trend of both Q and FOM remains consistent, with a minor discrepancy observed at 1010.5 nm. At this point, the growth rate of Q decreases, while the growth rate of FOM increases. However, after this point, the change slope becomes the same again, and both Q and FOM maintain a stable growth rate throughout the subsequent measurements. The minimum values of Q and FOM are 301.9 and 1.43 nm⁻¹, respectively, while the maximum values are 339.6 and 1.51 nm⁻¹. The median values are 320.2 and 1.47 nm⁻¹, respectively.

A proficient sensor requires appropriate LOD and DA values for assessing its performance metrics. This paper concentrates on pressure detection, thus warranting an examination of LOD and DA values in both forward and backward pressure detection scenarios. Fig. 11(a) displays the absorption rate's dependence on the incidence angle. During forward propagation, a solid red curve is observed, filled with a red and white gradient. Conversely, when EWs propagate backward, a dashed blue curve emerges, adorned with a blue and white gradient. To calculate DA , data points (18.05, 0.5), (21.85, 0.5), (77.75, 0.5), and (82.2, 0.5) from the figure are chosen. Employing Eqs.(23) and (24) in conjunction with the selected data points, we ascertain that the resonance angle difference ($\Delta\theta_{SPR}$) equals 3.8 for forward propagation and 4.45 for backward propagation. In Fig. 11(c) and (d), LOD and DA exhibit nearly identical trends. LOD demonstrates a conspicuous rise with increasing operating wavelength, elevating from 8.97×10^{-3} to 9.2×10^{-3} in Fig. 11(c). Nevertheless, the overall trend remains relatively stable, with a standard deviation of merely 1.067×10^{-4} . In stark contrast, DA values experience a substantial decline, decreasing from 3.878 to 3.77. Notably, at 558.7 nm, an evident peak value is observed, with $LOD = 9.23 \times 10^{-3}$ and $DA = 3.77$. This pattern persists in Fig. 11 (d), with LOD increasing from 1.514×10^{-2} to 1.563×10^{-2} , summing to 9.243×10^{-2} . Simultaneously, DA values decrease from 1.44 to 1.39, with a mean value of 1.41. In summary, the pressure sensing function of the structure demonstrates relatively robust performance.

Table 5 provides a comparative analysis showcasing the design features of the proposed sensor in this paper. In comparison to other sensors of the same type, our sensor exhibits superior S , Q , and FOM values. Additionally, it enables the simultaneous measurement of three different physical quantities. Notably, in the field of pressure sensing, the incorporation of multi-material and multi-directional sensing characteristics enhances the accuracy of practical applications. These advantages set

our sensor apart from existing sensors and demonstrate its potential for various applications.

5. Conclusion

In conclusion, a novel Janus LPS is proposed to act as a sensor, capable of simultaneously measuring angle, thickness, and pressure. To enhance the accuracy of pressure sensing, four different pressure-resistant materials are employed in the front and back directions, enabling data verification and improved sensing precision. The design process is optimized using EPSO to drive TMM calculations, resulting in superior performance. For forward incident EWs, the sensor demonstrates angular sensing capabilities with $S = 0.32$ nm/degree, $Q = 543.9$, and $FOM = 0.32$ degree⁻¹. Regarding pressure sensing, the S , Q , and FOM values are 5.46 nm/GPa, 563.9, and 5.5 GPa⁻¹, respectively. Similarly, the sensor maintains excellent performance in the backward direction, with $S = 10.24$ nm/GPa, $Q = 316.7$, and $FOM = 3.3$ GPa⁻¹. Additionally, the sensor effectively detects the deformation induced by pressure, yielding $S = 6.64$ and 4.7, $Q = 540.6$ and 320.1, and $FOM = 6.76$ nm⁻¹ and 1.47 nm⁻¹ for forward and backward measurements, respectively. These advantages are achieved by leveraging the powerful global optimization function of EPSO, which iteratively finds optimal models by physical laws. The EPSO and LPS-based Janus pressure sensor holds potential for diverse applications across various fields.

Declaration of Competing Interest

The authors declare that they have no known competing financial interests or personal relationships that could have appeared to influence the work reported in this paper.

Data availability

Data will be made available on request.

Acknowledgement

This work was supported by the College Student Innovation Training Program of Nanjing University of Posts and Telecommunications

Appendix A. Supplementary data

Supplementary data to this article can be found online at <https://doi.org/10.1016/j.optlastec.2023.110242>.

References

- [1] E. Yablonovitch, Inhibited spontaneous emission in solid-state physics and electronics, *Phys. Rev. Lett.* 58 (20) (1987) 2059.

- [2] S. Jena, R.B. Tokas, P. Sarkar, Omnidirectional photonic band gap in magnetron sputtered TiO₂/SiO₂ one-dimensional photonic crystal, *Thin Solid Films* 599 (2016) 138–144.
- [3] S.G. Johnson, J.D. Joannopoulos, Three-dimensionally periodic dielectric layered structure with omnidirectional photonic band gap, *Appl. Phys. Lett.* 77 (22) (2000) 3490–3492.
- [4] P. Mahesh, D. Panigrahy, C. Nayak, A comprehensive study of tunable properties of broadband terahertz absorber based on graphene-embedded random photonic crystals, *Phys. B Condens. Matter* 650 (2023), 414581.
- [5] S.S. Rao, Y. Zhou, B.F. Wan, Tunable polarization encoder capable of polarization conversion and separation based on a layered photonic structure, *IEEE J. Sel. Top. Quantum Electron.* 29(1) (2022). *Nonlinear Integrated Photonics*: 1–8.
- [6] T.W. Lu, P.T. Lee, Ultra-high sensitivity optical stress sensor based on double-layered photonic crystal microcavity, *Opt. Express* 17 (3) (2009) 1518–1526.
- [7] J.B. Maurya, A. François, Y.K. Prajapati, Two-dimensional layered nanomaterial-based one-dimensional photonic crystal refractive index sensor, *Sensors* 18 (3) (2018) 857.
- [8] A. Bijalwan, B.K. Singh, V. Rastogi, Analysis of one-dimensional photonic crystal-based sensor for detection of blood plasma and cancer cells, *Optik* 226 (2021), 165994.
- [9] A.K. Goyal, H.S. Dutta, S. Pal, Recent advances and progress in photonic crystal-based gas sensors, *J. Phys. D Appl. Phys.* 50 (20) (2017), 203001.
- [10] J. Xu, Z. Tang, Y.R. Wu, A multi-physical quantity sensor based on a layered photonic structure containing layered graphene hyperbolic metamaterials, *PCCP* 25 (26) (2023) 17558–17570.
- [11] H.A. Elsayed, A. Sharma, Z.A. Alrowaili, Theoretical investigation of pressure sensing using a defect of polystyrene inside photonic crystals, *Mater. Chem. Phys.* 270 (2021), 124853.
- [12] G. Teubner, The two faces of Janus: rethinking legal pluralism, *Cardozo L. Rev.* 13 (1991) 1443.
- [13] J. Sui, S. Liao, R. Dong, A Janus Logic Gate with Sensing Function, *Annalen der Physik* 535 (4) (2023) 2200661.
- [14] S.Y. Vetrov, R.G. Bikbaev, I.V. Timofeev, The optical Tamm states at the edges of a photonic crystal bounded by one or two layers of a strongly anisotropic nanocomposite, *Opt. Commun.* 395 (2017) 275–281.
- [15] S. Guo, C. Hu, H. Zhang, Unidirectional ultrabroadband and wide-angle absorption in graphene-embedded photonic crystals with the cascading structure comprising the Octonacci sequence, *JOSA B* 37 (9) (2020) 2678–2687.
- [16] C.J. Wu, Z.H. Wang, Properties of defect modes in one-dimensional photonic crystals, *Prog. Electromagn. Res.* 103 (2010) 169–184.
- [17] T. Zhan, X. Shi, Y. Dai, Transfer matrix method for optics in graphene layers, *J. Phys. Condens. Matter* 25 (21) (2013), 215301.
- [18] J. Kennedy, R. Eberhart, Particle swarm optimization, in: *Proceedings of ICNN'95-international conference on neural networks*. IEEE, 1995, 4, pp. 1942–1948.
- [19] Y.H. Wang, H.F. Zhang, Angular insensitive nonreciprocal ultrawide band absorption in plasma-embedded photonic crystals designed with improved particle swarm optimization algorithm, *Chin. Phys. B* 32 (4) (2023), 044207.
- [20] S.Y. Vetrov, R.G. Bikbaev, I.V. Timofeev, Optical Tamm states at the interface between a photonic crystal and a nanocomposite with resonance dispersion, *J. Exp. Theor. Phys.* 117 (2013) 988–998.
- [21] E.D. Palik, Gallium arsenide (gaas), "Handbook of optical constants of solids, Academic Press (1997:) 429–443.
- [22] D.J. Wilson, K. Schneider, S. Hönl, Integrated gallium phosphide nonlinear photonics, *Nat. Photonics* 14 (1) (2020) 57–62.
- [23] I.H. Malitson, Interspecimen comparison of the refractive index of fused silica, *Josa* 55 (10) (1965) 1205–1209.
- [24] S. Brown, A. Marshall, P. Hirst, The growth of single crystals of lead molybdate by the Czochralski technique, *Mater. Sci. Eng. A* 173 (1–2) (1993) 23–27.
- [25] M. Danaie, H. Kaatuzian, Design and simulation of an all-optical photonic crystal AND gate using nonlinear Kerr effect, *Opt. Quant. Electron.* 44 (2012) 27–34.
- [26] S. Rao, H. Fu, J. Zhang, Tunable phase retarder of 1D layered photonic structure combining nonlinear Kerr dielectric defect layers and magnetized plasma materials, *Annalen der Physik* 534 (11) (2022) 2200337.
- [27] P.G. Huray, Maxwell's equations, John Wiley & Sons, 2011.
- [28] B.F. Wan, Z.W. Zhou, Y. Xu, A theoretical proposal for a refractive index and angle sensor based on one-dimensional photonic crystals, *IEEE Sens. J.* 21 (1) (2020) 331–338.
- [29] F. Ghasemi, S.R. Entezar, S. Razi, Terahertz tunable photonic crystal optical filter containing graphene and nonlinear electro-optic polymer, *Laser Phys.* 29 (5) (2019), 056201.
- [30] M.S. Kumar, S. Menabde, S. Yu, Directional emission from photonic crystal waveguide terminations using particle swarm optimization, *JOSA B* 27 (2) (2010) 343–349.
- [31] Q. Ma, X. Lei, Q. Zhang, Mobile robot path planning with complex constraints based on the second-order oscillating particle swarm optimization algorithm, in: *2009 WRI world congress on computer science and information engineering*, IEEE, 2009, 5, pp. 244–248.
- [32] B.F. Wan, Q.Y. Wang, H.M. Peng, H.N. Ye, H.F. Zhang, A Late-Model Optical Biochemical Sensor Based on OTS for Methane Gas and Glucose Solution Concentration Detection, *IEEE Sens. J.* 21 (19) (2021) 21465–21472.
- [33] S. Pezzagna, J. Brault, M. Leroux, Refractive indices and elasto-optic coefficients of GaN studied by optical waveguiding, *J. Appl. Phys.* 103 (12) (2008).
- [34] B. Suthar, A. Bhargava, Pressure sensor based on quantum well-structured photonic crystal, *SILICON* 13 (6) (2021) 1765–1768.
- [35] M. Huang, Stress effects on the performance of optical waveguides, *Int. J. Solids Struct.* 40 (7) (2003) 1615–1632.
- [36] S. Dinodiya, A. Bhargava, A comparative analysis of pressure sensing parameters for two-dimensional photonic crystal sensors based on Si and GaAs, *SILICON* 14 (9) (2022) 4611–4618.
- [37] S. Dinodiya, A. Bhargava, A comparative analysis of pressure sensing parameters for two dimensional photonic crystal sensors based on Si and GaAs, *SILICON* 14 (9) (2022) 4611–4618.
- [38] Z. Xiong, L. Shang, J. Yang, Terahertz sensor with resonance enhancement based on square split-ring resonators, *IEEE Access* 9 (2021) 59211–59221.
- [39] N.L. Kazanskiy, S.N. Khonina, M.A. Butt, A numerical investigation of a plasmonic sensor based on a metal-insulator-metal waveguide for simultaneous detection of biological analytes and ambient temperature, *Nanomaterials* 11 (10) (2021) 2551.
- [40] B. Sun, Y. Yu, W. Yang, Enhanced toroidal localized spoof surface plasmons in homolateral double-split ring resonators, *Opt. Express* 28 (11) (2020) 16605–16615.
- [41] Z. Y. Zhang, F. Fan, T. F. Li, Y. Y. Ji, S. J. Chang, Terahertz polarization conversion and sensing with double-layer chiral metasurface, *Chin. Phys. B* 29(7) (2020) 07870.
- [42] J. Xu, T.Q. Zhu, H.F. Zhang, Multi-physical Quantity Sensing Based on Magnetized Plasma Spherical Photonic Crystals with Evanescent Wave, *J. Phys. D Appl. Phys.* (2023).
- [43] M.S. Rahman, K.A. Rikta, L.F. Abdulrazak, Enhanced performance of SnSe-Graphene hybrid photonic surface plasmon refractive index sensor for biosensing applications, *Photonics Nanostructures-Fundamentals Appl.* 39 (2020), 100779.